# Broadspectrum InGaAs/InP Quantum Well Infrared Photodetector via Quantum Well Intermixing

Deepak Sengupta*, Yia-Chung Chang, and Greg Stillman

Department of Electrical & Computer Engineering and Department of Physics,

University of Illinois at Urbana-Champaign, 1406 W. Green Street, Urbana, IL 61801

## Abstract

We have demonstrated red shifting and broadening of the wavelength response of a bound-to-continuum ultra-thin p-type InGaAs/InP quantum well infrared photodetector (QWIP) after growth via quantum well intermixing. A substantial bandgap blue shift, as much as 292.5 meV at 900°C have been measured and the value of the bandgap shift can be controlled by the anneal time. Compared to the as-grown detectors, the peak spectral response of the intermixed detector was shifted to longer wavelengths without any major degradation in the responsivity characteristics. In general, the overall performance of the intermixed QWIP has not dropped significantly, with the spectral broadening taken into account. Thus, the post-growth control of the quantum well composition profiles offers unique opportunities to fine tune various aspects of a photodetector's response. Theoretical modeling of the intermixing effect on the energy levels is performed based on the effective bond-orbital method and obtain a very good fit to the photoluminescence data.

(* presently with the Jet Propulsion Laboratory, Pasadena, CA 91109)

## Introduction

Since the first proposal of the semiconductor multiple quantum wells (MQW's) by Esaki and Tsu [1], there have been extensive theoretical and experimental studies on this subject. To date, lattice-matched MQW's including GaAs-$Al_xGa_{1-x}As$, InAsGaSb, $In_xGa_{1-x}As$-InP, $Ga_{1-x}In_xAs$-$Al_{1-x}Ga_xAs$ can be grown by molecular beam epitaxy (MBE) with nearly perfect interface quality [2-5]. Good quality strained-layer superlattices [6] have recently been successfully grown. These include Ga (As,P), Ga (As,Sb), (Al,Ga) Sb, (In, Ga,Al)As, and Si-Ge systems [7-9]. Detailed information about the electronic, optical, and transport properties of semiconductor MQW's has been accumulated via various experimental techniques [10-14]. Theoretically, many sophisticated methods have been used to calculate the electronic band structures and optical properties of these systems. These include psuedopotential [15,16] tight-binding [17-19], effective mass [20-22], k.p [23], wannier-orbital [24], and bond-orbital [25] methods. With all of these efforts, fundamental physical phenomena such as excitonic excitation, electron and hole tunneling, impurity states, quantum stark effect, lattice vibrations, electron-phonon coupling, inter-subband transitions, and quasi-two dimensional plasma are more or less understood. With ample knowledge about the fundamental physical phenomena available to us, we have reached the stage where the combination of experimental characterization with detailed theoretical analysis can now provide meaningful engineering design of quantum well devices that will find immediate application. Some of the more successful applications include quantum-well lasers[26-28], optical switches [29-31], photodetectors [32-34], and optical modulators [35-37].

In recent years, considerable interest has focused on the fabrication and characterization of III-V based quantum well infrared photodetector. [38]. Modern photoconductive quantum well infrared photodetectors, with responses at various wavelengths from 5-12μm, were first demonstrated by B.F. Levine et.al. in 1987 [39]. A schematic of the

type I quantum well structure is shown in Fig. 1. In most QWIP devices, a signal is generated when a quantum well absorbs infrared radiation. This excites electrons from the ground state to an excited state from which the excited electron is collected by an applied field, resulting in photocurrent. The use of these materials rather than conventional mercury cadmium telluride(MCT) detector is based upon two advantages:
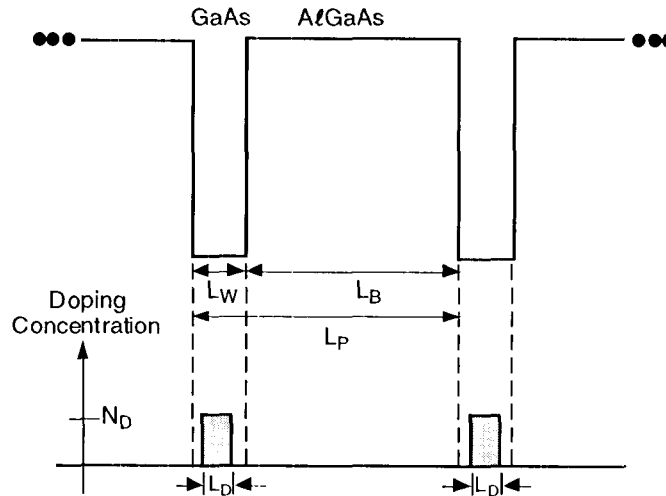


$L_W$ = Well width (40Å)

$L_B$ = Barrier width (300Å)

$L_P$ = Width of one period of the structure (340Å)

$L_D$ = Width of intentionally doped region in the quantum well (center 20Å of quantum well)

$N_D$ = Doping concentration intentionally introduced in the quantum well over a region of width $L_D$ (1.0 x $10^{18}$/cm$^3$)

Fig. 1. Schematic drawing of the type I quantum well structure. The parameters for the standard structure are indicated above.

First, these detectors are fabricated from GaAs/Al$_x$Ga$_{1-x}$As quantum well superlattices, a significantly less expensive, more uniformly grown and more abundant material than MCT. Second, standard high yield GaAs integrated circuit fabrication techniques may be used, paving the way for advanced sensor arrays and their cost effective manufacture

with existing infrastructures. The price paid for the easy fabrication of QWIPs is that they have lower quantum efficiency and higher dark current than ideal narrow gap detectors such as MCT [40]. The many fabrication problems in MCT make it generally unsuitable for a large array technology or monolithic integration. Here is where QWIPs find their niche. The GaAs/A1$_x$Ga$_{1-x}$As QWIP is easier to fabricate, less expensive to grow, and     uniform across large area two-dimensional (2-D) arrays at low cost. Long-wavelength imaging systems such as the 15μm cut-off 128 x 128 QWIP FPA camera, 256 x 256 Portable QWIP FPA camera, 9μm cut off 640 x 436 QWIP FPA camera, and 256 x 256 Palm size QWIP FPA camera have been demonstrated by the Jet Propulsion Laboratory and achieved an excellent imagery with a noise equivalent differential temperature of $_\wedge$ 15 mK [41]. Superlattice detectors are therefore extremely versatile due to the nearly limitless possibilities of bandgap engineering (three fundamental structures: bound-to-bound, bound-to-continuum, and bound-to-miniband). Besides the successful GaAs/A1$_x$Ga$_{1-x}$As superlattice, other III-V materials have indicated promise as LWIR detectors. Incremental engineering advancements are quickly changing the perspective on QWIP, towards one of great hope, as its successor to MCT in LWIR array technology. Cost issues affect the development and function commercialization of such technology.


In spite of the successful developments of intersubband GaAs/A1$_x$Ga$_{1-x}$As QWIP technology, only little effort has focused on broadspectrum / multi-color detection using the InGaAs/InP material system [42]. The InGaAs/InP material system [43] has the advantage of binary InP barriers which have the potential for improved barriers quality and transport. This implies a lower dark current relative to the GaAs/A1$_x$Ga$_{1-x}$As material system which has ternary barrier employing aluminium. Also due to the high quality InP barriers, lattice matched InGaAs/InP ternary may have superior properties compared to GaAs/AlGaAs QWIPs. Apart from the excitation of electrons, using holes in the

InGaAs/InP system offers three potential advantages: The first is a reduction in the dark current. The larger mass of the holes in the InGaAs/InP system relative to the mass of electrons, leads to lower tunneling probability and therefore lower dark currents. The second advantage is that a broader spectral response can be achieved. In the plane of the well, the energy-momentum relation for holes is not a single parabola, as in the case of electrons, and therefore absorption from one subband to another does not occur at the same transition energy for all hole moments. This results in a broadening of the absorption spectrum which is beneficial for broad spectral imaging. Finally, most of the GaAs/AlGaAs bandgap discontinuity is in the conduction band, whereas in InGaAs/InP p-QWIP intersubband absorption can occur at a much shorter wavelength.

Modifying the layer (i.e., quantum well and/or barrier width) thickness will change the absorption wavelengths of the raw material. In this manner, one can grow detectors which are tuned for absorption at various wavelengths. This method, however, relies on a separately grown superlattice, possibly on different substrates for each different absorption peak wavelength desired. An alternative method to achieving variation in absorption peaks which can easily be employed is the technique known as impurity-free vacancy disordering. In this case, a dielectric cap layer is deposited on top of the structure followed by a rapid thermal anneal process [44, 45, 46, 47]. Such tunability is of potential interest for infrared detector applications as it would facilitate the fine-tuning of the peak detector response of as-grown structures to a desired operating wavelength. In addition, rapid thermal annealing can be used to broadened spectral responses, a direct result of the linear super position of adjacent absorption maxima and as well as multiple-color detections by shifting each detector by different amount.

In this article, we describe the growth and characterization of 4.55 $\mu$m p-doped InGaAs/InP QWIPs and the optical and device studies of the effect of intermixing on an

ultra-thin (~ 10 Å) p-type InGaAs/InP multiple quantum well structures using $SiO_2$ coping. Finally, theoretical calculations based on the effective band-orbital method is performed to compare with the experimental results. We first present the details of our experiments and measurements procedures. Next, a brief discussion of our theoretical calculations is conducted, and the model is compared to experimental data.


Growth and Material Characterization of an Ultra-Thin P-Type InGaAs/InP QWIP

Epitaxial growth was performed in a modified Perkins-Elmer 430P gas source molecular beam epitaxy (GSMBE) system [48]. The growth chamber was equipped with a 5000 $\ell$/s cryopump and a 200 $\ell$/s turbo molecular pump. Cracked $AsH_3$ and $PH_3$ (>99%) were used as the group V sources, while elemental solid sources in effusion cells were used for the group III sources. Cracked $AsH_3$ and $PH_3$ were injected separately from two independent low-pressure crackers equipped. Switching of $ASH_3$ and $PH_3$ was controlled by the fast vent/run valves in front of each injector. Details of the MBE system and cracker design are reported elsewhere [48]. p-type InGaAs/InP QWIP structure were grown on semi-insulating (001) InP substrates at 500°C. InP was grown at a rate of 0.59 μm/hr with a $PH_3$ flow of 2-5 sccm, and lattice-matched $Ga_{0.47}In_{0.53}As$ was grown at 1.05 μm/hr with an $AsH_3$ flow of 2.5 sccm. Growth chamber pressure with hydride gas flowing was 2 x $10^{-6}$ torr as measured by a cold cathode gauge. The pressure reached the gauge baseline value of <$10^{-7}$ torr approximately 7 seconds after hydride gas flow was switched from the growth chamber into the vent lines. The p-type structure shown in Fig. 2 consisted of 30 periods of 10 Å Be center doped (3 x $10^{18}$ cm$^{-3}$) $In_{0.53}Ga_{0.47}As$ quantum wells (QWs) and 500 Å Be doped (1 x $10^{17}$ cm$^{-3}$) InP barriers sandwiched between 5000 Å Be doped (3 x $10^{18}$ cm$^{-3}$) $In_{0.53}Ga_{0.47}As$ contacts on InP substrate. The material quality of the p-type InGaAs/InP quantum wells were investigated using double crystal X-ray diffraction and cross-sectional scanning tunneling microscopy. In the case of p-type InGaAs/InP QWIPs, for each type of interface, normal (InGaAs-on-InP) and

| | |
|---|---|
| 5000 Å InGaAs : Be $3 \times 10^{18}$/cm$^3$ | |
| 500 Å InP : Be $1 \times 10^{17}$/cm$^3$ | |
| 10 Å InGaAs : Be $3 \times 10^{18}$/cm$^3$ | x30 |
| 500 Å InP : Be $1 \times 10^{17}$/cm$^3$ | |
| 5000 Å InGaAs : Be $3 \times 10^{18}$/cm$^3$ | |
| 3000 Å InP : UNDOPED BUFFER LAYER | |
| InP : Fe SUBSTRATE | |

Fig. 2. Structure of InGaAs/InP p-type QWIP.

inverted (InP-on-InGaAs), a different source switching scheme was used [48]. A two-step procedure was implemented for InGaAs-on-InP interface. Growth of InP was terminated by closing the In shutter and switching the $PH_3$ flow from the growth chamber to a vent line. Thus the InP surface remained free of any flux for fixed period of time, $T_P$ seconds. Then $AsH_3$ was introduced into the growth chamber exposing the InP surface to $As_2$ overpressure for $T_{As}$ seconds before the growth of InGaAs, providing longer $P_2$ pumping time to remove the phosphorous while preserving the InP surface from degradation. Growth was resumed after the completion of a second time period by opening the Ga and In shutters. Growth of InGaAs was terminated by closing the In and Ga shutters. Simultaneously, the flow of $AsH_3$ was directed from the growth chamber to the vent line. Thus, no flux or overpressure was applied to the InGaAs surface to $T_{As}$ seconds. During this time, residual arsine was pumped from the growth chamber. Growth was resumed after the completion of the $T_{As}$ interval by opening the in shutter and flowing $PH_3$ into the growth chamber. Various combinations of the three times $T_P/T_{As}/T_{As}$ were applied to the growth of the samples, and the optimized times 7/10/20 were established based on the photoluminescence and DCXRD measurements.

DCXRD measurements were carried out to characterize the crystalline quality of the p-type InGaAs/InP superlattice layer (SL). A Phillips double-crystal X-ray diffractometer

was used to measure the diffraction patterns. Each of the diffraction patterns were measured in a θ-2θ mode with a fine collimation of the incident and diffracted X-rays in order to track the evolution of its superlattice harmonics over several degrees. Fig. 3 (a) shows the experimented and simulated (004) CuKα1 rocking curves of the p-QWIP structure with 30 periods of InGaAs/InP SL (10 Å InGaAs well and 500 Å InP barrier). The superlattice satellites are observed up to the 4th order, and the average FWHM of the experimental satellite peaks is 31 arcsec., demonstrating excellent material quality. The simulation in Fig. (b) assumed abrupt interfaces for both InGaAs-on-InP and InP-on-InGaAs interfaces, and that in Fig. (c) assumes a monolayer of $InAs_{0.5}P_{0.5}$ inserted at the upper interfaces of the InGaAs layer. Clearly, a transitional monolayer in the group V sublattice gives a much better agreement than the abrupt interface does between experiment and simulation, suggesting residual $As_2$ incorporation in the InP layers and formation of strained monolayers at the interfaces. In this case, a period consists of three layers: 10.5 Å $In_{0.475}Ga_{0.525}As$, 3.04 Å $InAs_{0.5}P_{0.5}$ and 564.3 Å InP and to atomic layer schematic can be expressed as In-P-In-P*-GaIn-As-GaInAs-GaIn-As*-In*AsP*-In-P-In-P.


Fig. 4 shows cross-sectional scanning tunneling microscope (XSTM) image of InP/InGaAs p-QWIP structure with ultra short quantum wells [49]. The InP barrier appears darker than the adjacent InGaAs well region because of its valence band offset. The InGaAs regions also have a mottled appearance due to alloy fluctuations. A marked difference in roughness between the normal and inverted interface was observed. As shown in Fig. 4, the normal interface is extremely sharp, with the intermixing within a monolayer in the [001] direction. The roughness observed at the inverted interface can be attributed to:
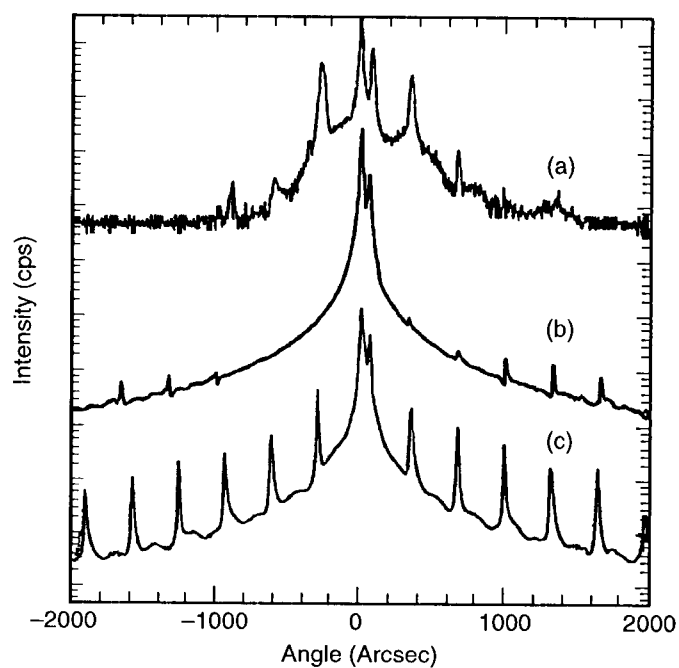
Fig. 3. High resolution double-crystal x-ray diffraction rocking curves of a 30-period InGaAs/InP QWIP structure. (a) Experimental rocking curves of the p-type QWIP structure (b) Simulation assuming abrupt interface for both InGaAs-on-InP and InP-on-InGaAs interfaces; (c) Simulation assuming a monolayer of $In_{0.5}As_{0.5}P$ inserted at each inverted interface.
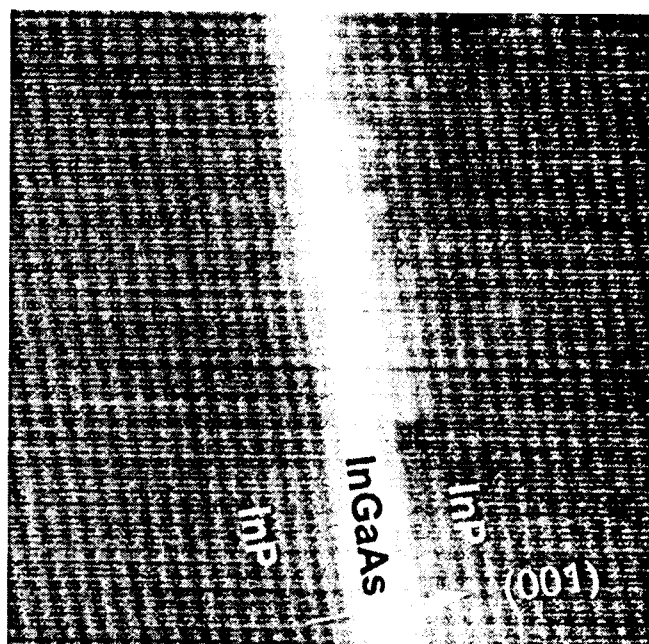


Fig. 4. Cross-sectional scanning tunneling microscopy (XSTM) of a p-type InGaAs/InP QWIP with about 4 to 5 monolayers within quantum well.

1. Alloy fluctuations within the InGaAs.

2. The exchange of group V species. Due to the large chemical binding energy difference between As and P compounds, the exchange and diffusion of group V species is expected during the growth interruption. Because of larger binding energy (GaP > GaAs), the exchange and diffusion of P into InGaAs is likely and the diffusion rate of P is typically much higher than that of As. DCXRD measurements on InGaAs/InP (GaAs/InGaP) interfaces suggest partial exchange of As with P within the first 3-4 InGaAs (GaAs) monolayers during exposure to a $P_2$ beam.

3. The residual $As_2$ incorporated into the InP layers. Since $As_2$ has a larger incorporation coefficient than $P_2$, even a little amount of residual $As_2$ in the growth chamber will cause the carryover of As into InP layer, forming InAs(P) layer. As shown in Fig. 5, higher density of As and scattered As atoms were observed at the inverted interface and in the first 5-6 InP monolayers, respectively. In addition to providing direct evidence of well-defined quantum wells, barriers, and interfaces, the XSTM results allowed independent determination of the thicknesses for later comparison to results derived from DCXRD rocking curve fits calculated using dynamical theory.


## Red-Shifting and Broadening via Quantum Well Intermixing

The bandgap tuning of multi-quantum well structures requires changing the bandgap spatially across the wafer. One way to reach the goal is to use the technique of intermixing via rapid thermal annealing. This process modifies the geometry and composition of QWs and leads to a blue shifted bandgap. The post-growth wavelength shifting of QWIPs by rapid thermal annealing is accomplished by dielectric encapsulation of the QWIP and exposing it to a high temperature for a short period of time. The quantum well is changed from a square well with a sharp interface, to an error-function

shaped well with a corresponding change in the confined energy levels. The redistributed profile makes the quantum well thinner at the bottom than to originally grown well, shown in Fig. 6 (a).

This modification of the well width shifts the absorption to longer wavelengths as the energy level rises in the well. Dielectric film stress, transferred to the surface of the substrate, influences the amount of diffusion induced wavelength shifting which will occur during annealing. Deposition may take place via chemical vapor deposition (CVD), plasma enhanced chemical vapor deposition (PECVD), or sputtering. Substrate temperature, reactant gas composition, and for PECVD, microwave power applied to the plasma will change the film characteristics. Films such as silicon dioxide and silicon nitride, with their myriad of compositions and mixtures should be adequate to provide a wide intermixing of the interface in bit layer chambers. The annealing operation may be performed via rapid thermal annealing (RTA). Once the anneal is complete, the dielectric cap layer may be stripped and the wafers prepared for subsequent detector processing. Broad-spectrum/multi-color detection makes use of the variation in wavelength shift for different dielectric induced stress Fig 6(b), 6(c) and 6(d) illustrates that the broad spectrum response is a direct result of the linear super position of two adjacent absorption maxima. In all studies, prior to annealing the samples were first degreased in trichlorethane, acetone, and methanol followed by a light surface etch using $NH_4OH$. Then, a 1500Å $SiO_2$ encapsulant was deposited by plasma enhanced chemical vapor deposition. Rapid thermal annealing was performed in an AET RTA reactor with 10 sccm of $N_2$ flowing. The temperature was stabilized at 200°C prior to the high temperature annealing.
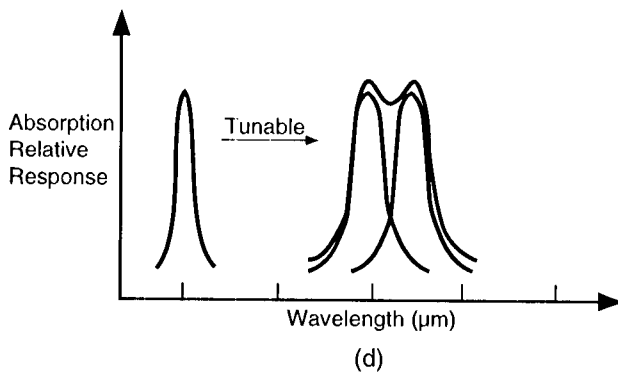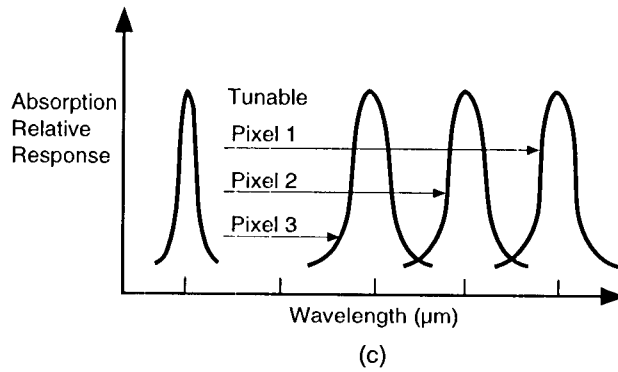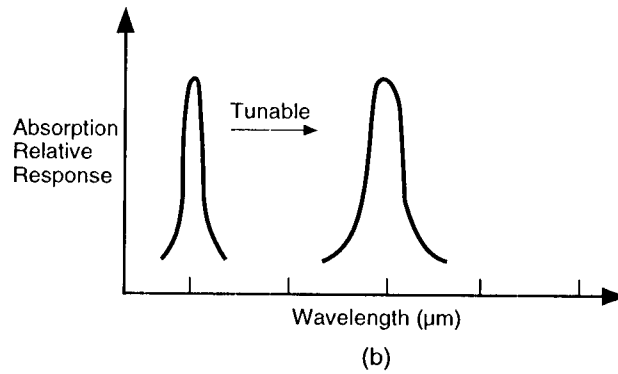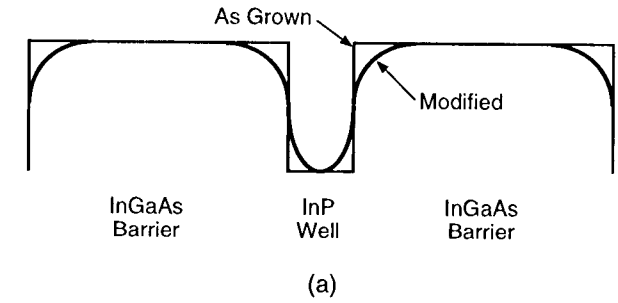
Fig. 6. (a) Modification of quantum well profile due to QW-intermixing. (b) Schematic representation of shifting effect and its utility for response detector tuning. (c) Multi-color detection by shifting each pixel a different amount. (d) Schematic representation of a broadband detector made possible through the linear superposition of the relative absorption response of two neighboring peaks.

The cross-sectioned TEM micrographs are shown in Fig. 7 for (a) an as-grown MQW and (b) an RTA MQW annealed at 800°C for 30 seconds. No defects or dislocations are observed for both as-grown and annealed MQW regions.



InP

InGaAs

InP

(a) As Grown          (b) 800C Annealing
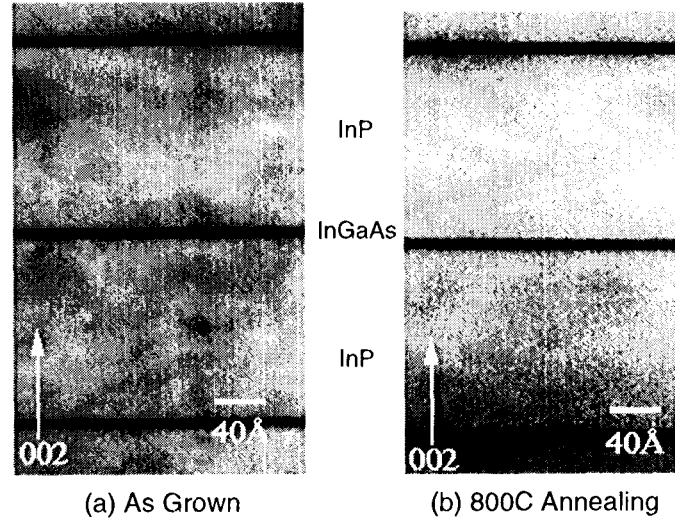
Fig. 7. Cross-sectional TEM of the (a) as-grown, and (b) RTA (800°C for 30s) MQW structures.

In Figure 8, the 6K PL spectrum of as-grown and annealed InGaAs/InP QWIP samples are shown. A blue shift (~24.0 meV @ 700°C, ~130.2 meV @ 800°C and ~292.5 meV @ 900°C) of photoluminescence peak was observed. This is expected, as the grown state is higher and the effective barrier height lower for the annealed QWIP than the as-grown QWIP. In addition to the blue shift, the annealed QWIP samples also exhibit a reduction in the peak luminescent intensity and is attributed to the out-diffusion of the p-type (Be) dopants from the well and is strongly dependent on the amount of disordering during the annealing process. Rapid thermal annealing at 900°C leads to a blue shift of ~292.5 meV and almost complete alloying. In Figure 9, the energy shift of the luminescence line is displayed against the corresponding annealing temperature for both as-grown and rapid
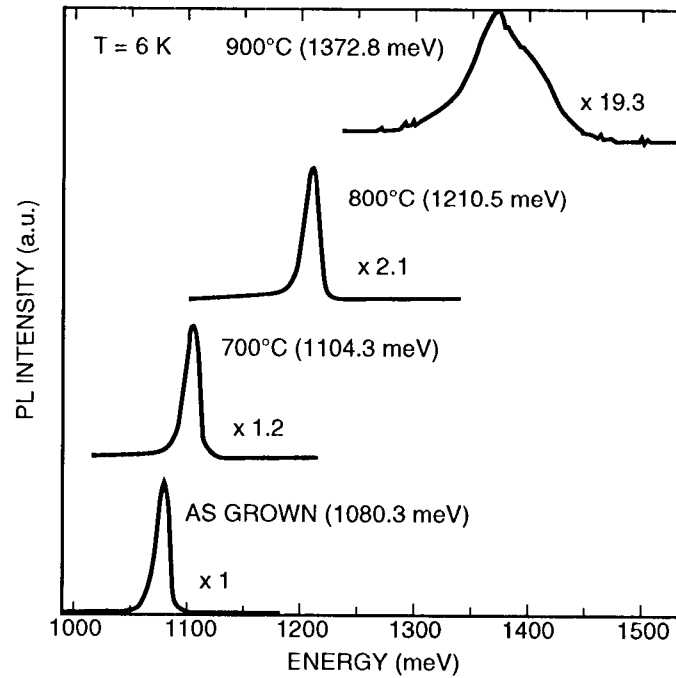
Fig. 8. Photoluminescence spectra at 6K of the as-grown and RTA (700°C, 800°C, and 900°C for 30s) MQW structures.
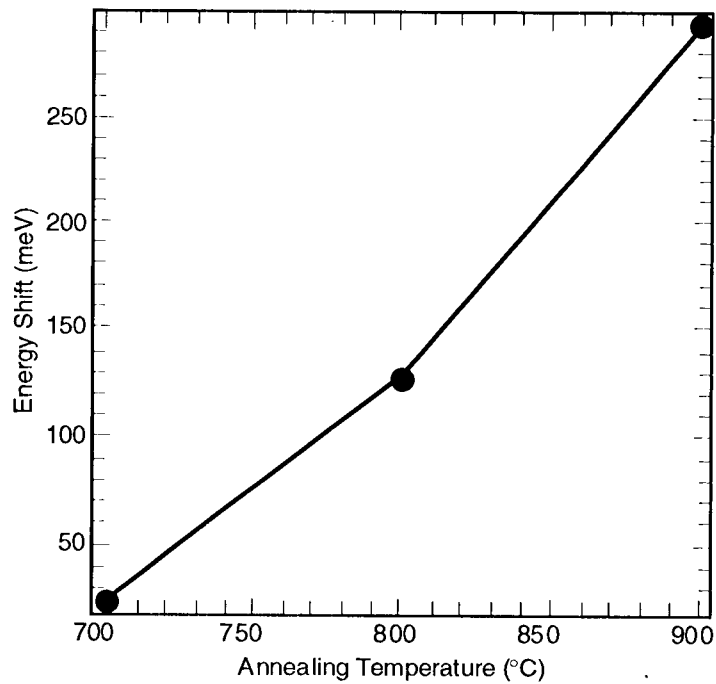


Fig. 9. Energy shift of the photoluminescence peak versus RTA (700°C, 800°C, and 900°C for 30s) MQW structures.

thermally annealed MQW investigated. The change of the emission energy is very pronounced. It is ~10Å quantum well, a small narrowing of the effective width causes a significant blue-shift due to the well width dependence of the first subband energies. In Figure 10, 6K PL spectrum of the as-grown and annealed (800°C) InGaAs/InP QWIP samples at 20, 40, and 60 sec are shown. A blue shift (~108 meV for 20 sec, ~135 meV for 40 sec and ~150 meV for 60 sec) of the photoluminescence peak was observed. Figures 11 and 12 show the integrated PL intensities and half width of the emission line versus the annealing temperatures. Up to an annealing temperature of 800°C, the half width of the luminescence spectrum remain approximately 19.3 to 19.6 meV and results in no significant degradation of the PL linewidth up to 800°C rapid thermal annealing.

In summary, we have achieved strong and homogeneous intermixing in InGaAs/InP MQWs, using $SiO_2$ capping and subsequently annealing. No significant degradation of
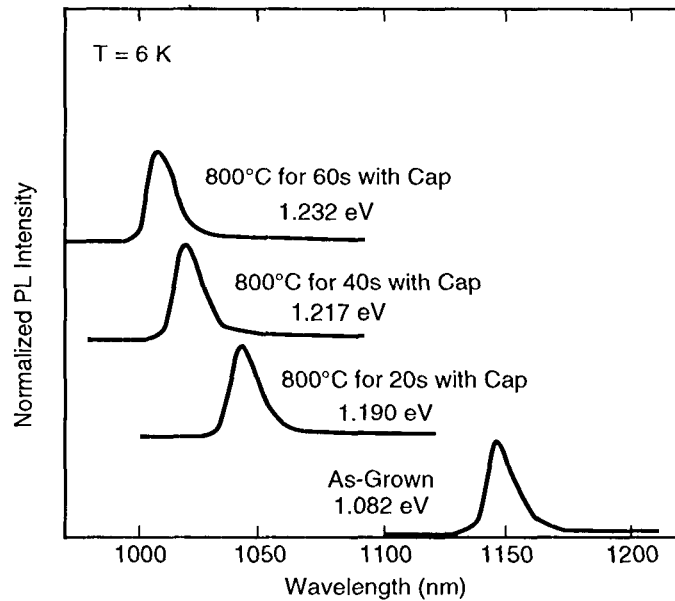


Fig. 10. 6K photoluminescence spectra of the as-grown and RTA treatment (800°C for 20, 40, and 60s).
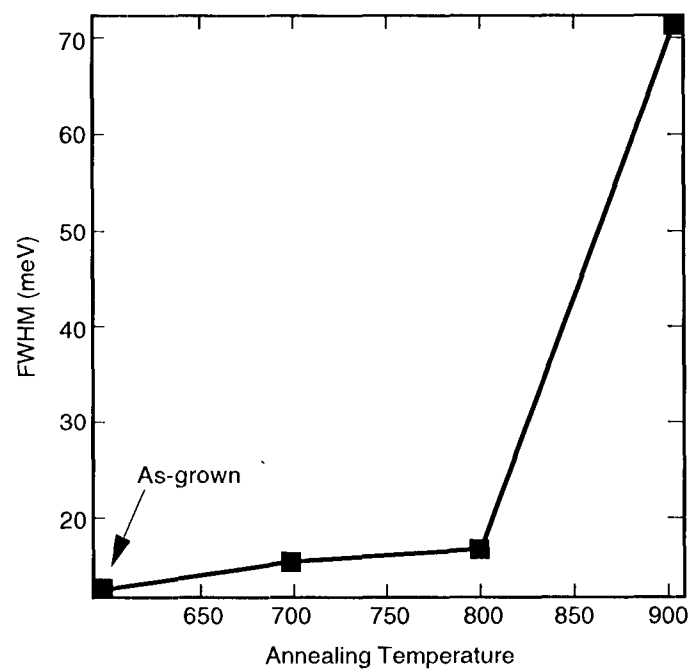
Fig. 11. 6K photoluminescence linewidth of the as-grown and RTA (700°C, 800°C, and 900°C for 30s) MQW structures.
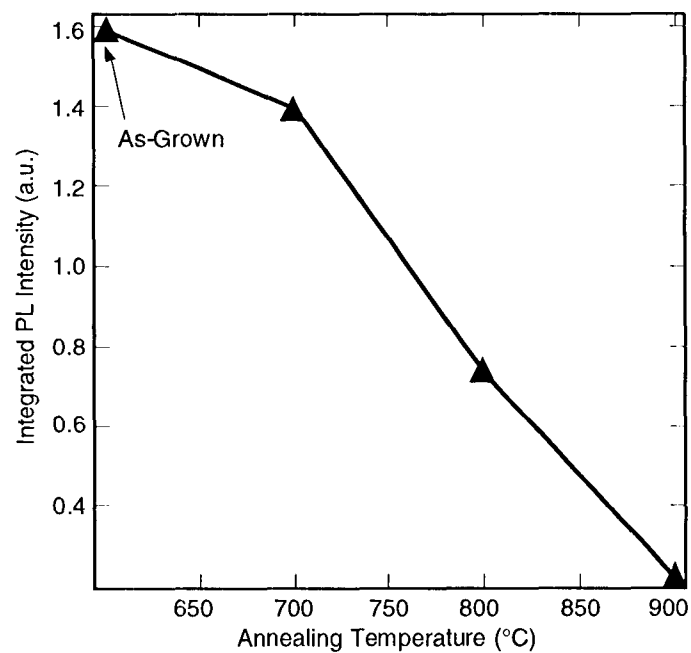


Fig. 12. 6K photoluminescence integrated PL intensities of the as-grown and RTA (700°C, 800°C, and 900°C for 30s) MQW structures.

optical properties was observed up to 800°C. A substantial PL blue shift, as much as 130.2 meV, was found in the structure and the value of the shift can be controlled by its anneal time. In addition, beyond 800°C annealed QWIP structure also exhibits a reduction in peak luminescent intensity, which may be due to the overall broadening of the peak response as well as any defects the annealing process might have introduced.


## Device Fabrication and Characterization

QWIPs were fabricated into 200 $\mu$m diameter mesa diodes by chemically etching and evaporating Ti/Pt (p-type) contacts. Devices were polished with 45° bevels (to accommodate selection rules) and indium bonded to a copper heat sink. The I-V measurements were done with a Keithley source measure unit and a two-stage closed cycle refrigerator. The sample was fully cold shielded. The detector response spectrum was taken with a Bomem Fourier Transform Spectrometer. The responsivity calibration was made using a 1000 K blackbody source and a narrow band pass filter.


The temperature dependent current-voltage curves both with full cold shielding and with $2\pi$ Sr 300 K background of the p-type InGaAs/InP QWIP are shown in Figs. 13(a) and (b), respectively. The dark current was observed to be insensitive to temperature changes up to 60 K. The dark current decreased significantly as the temperature was lowered due to the decrease of thermionic emission of carriers from the QWs at higher temperatures. It is also worth noting that for these QWIPs, the positive bias direction (defined mesa top positive) is the low dark current direction. That is, for both cases, the lowest dark current direction is composed of carriers flowing into the substrate.


In Figs. 14(a,b), on a log scale, we plot the normalized dark current (Id/T) measured at a bias of 50 mV, against the inverse temperature for the sample with peak response of
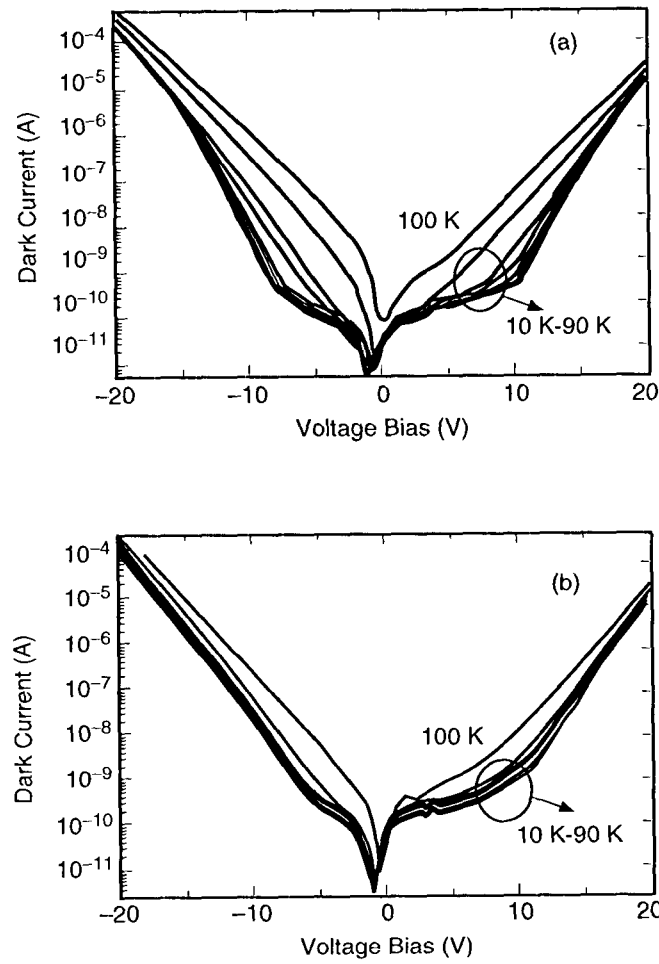
Fig. 13. Dark current versus bias for temperatures from 10 to 100 K for the p-type InGaAs/InP QWs with (a) full cold shielding and (b) $2\pi$ Sr 300 K background.

4.55 µm for the p-type InGaAs/InP. The excellent fit over several orders of magnitude in current yields activation energy $E_a$ corresponding to wavelength ~4.25 µm and 5.0 µm for the p-type InGaAs/InP. This is in good agreement with the optically measured peak response. This demonstrates that there is negligible tunneling contribution to the dark current, and thus the barriers are nearly ideal in their current blocking.

The bias dependence of the 45° incidence responsivity is shown in Fig. 15 for the p-type InGaAs/InP. An increase in response is observed with bias voltage and the peak
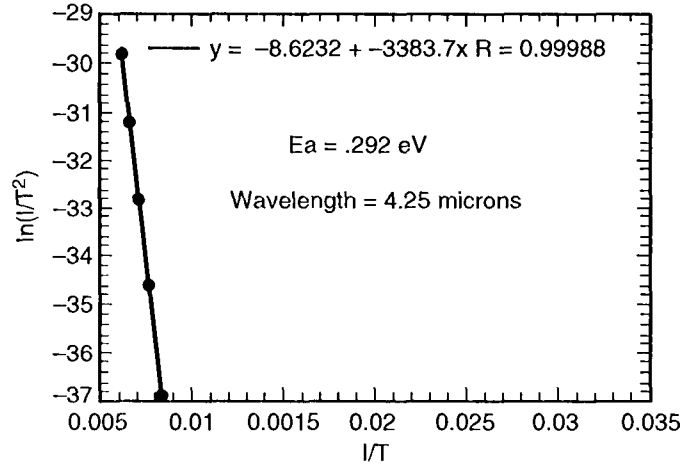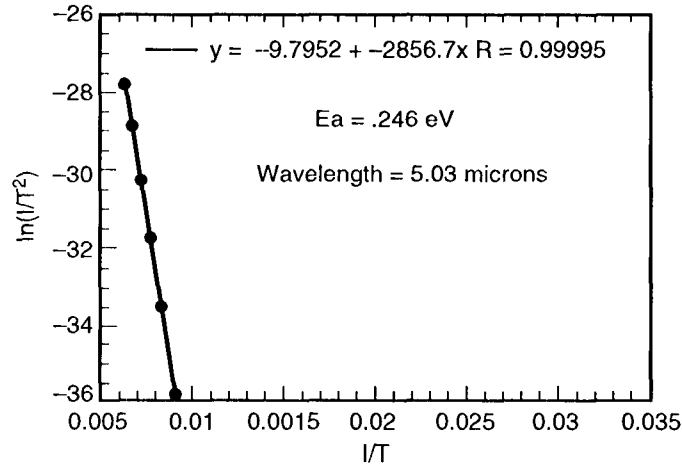
**Fig. 14.** Arrhenius plot of a p-type InGaAs/InP QWIP under (a) forward and (b) reverse biases. The activation energies correspond to wavelengths of ~4.25 and 5 μm, respectively.

wavelength shifts slightly with bias. The increase in response with bias is attributed to the step-like increase in the number of QWs included in the high field bias regime.

Figs. 15 & 16 show the photoresponse for both the as-grown and RTA detector with bias. The peak response wavelengths measured are ~4.55 μm (80K and 5.9V) for the as-grown
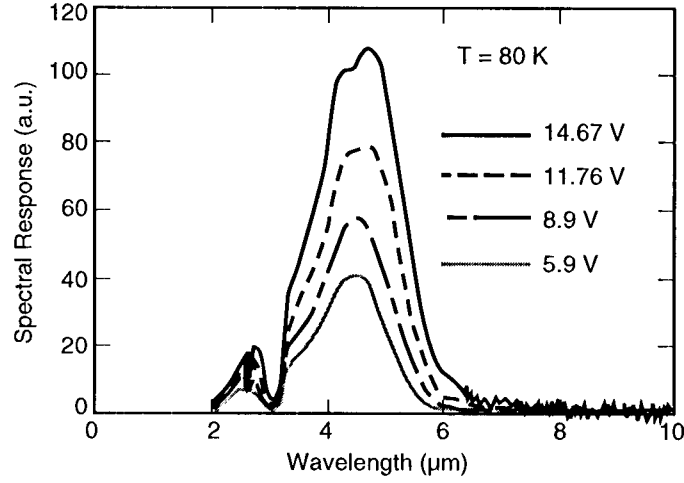
Fig. 15. Bias dependence of the spectral response for the as-grown QWIP at 80K.

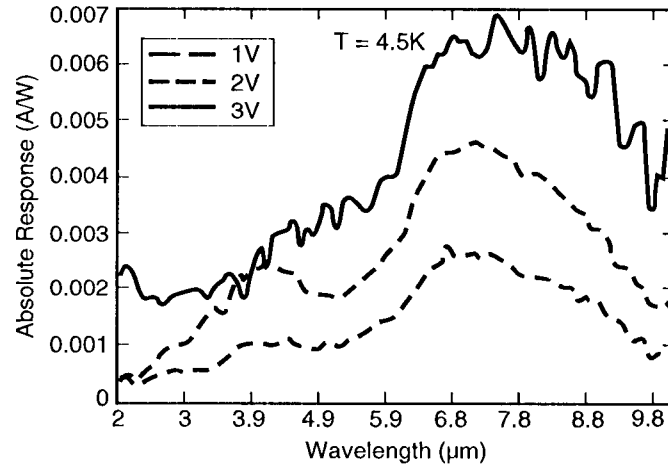

Fig. 16. Bias dependence of the spectral response measured for the RTA QWIP at 4.5K.

detector and ~7.0 μm (4.5K and 4V) for the RTA detector. Since the ground state is higher and the effective barrier height is lower in the RTA detector than in the as-grown detector, the peak response wavelength of the RTA detector experiences a long wavelength shift. The peak absolute responses are calculated to be ~2.5 mA/W (80K and 5.9V) for the as-grown detector and ~2.0 mA/W (4.5K and 4V) for the RTA detector from the blackbody and relative spectral response measurements. The peak responsivity

of the RTA detector is of a similar magnitude compared to the as-grown detector. Although the broadened absorption spectrum of the RTA detector can result in a reduced spectral response, we believe that the dominant reduction is a consequence of the out-diffusion of the Be dopant from the well and the increased dark current from the RTA detector structure. The small reduction in the response may still be acceptable for the focal plane array detector applications.


## Comparisons with Theory

Theoretical modeling of the intermixing effect on the energy levels is performed based on the effective bond-orbital method (EBOM). This method casts the k.p formalism into a local-orbital formalism so that the complicated boundary conditions in heterostructures can be easily managed. Details of this method is given in Ref. [50]. This method has been used to calculate the electronic structures and optical responses of many kinds of multiple quantum wells (MQW's), including GaAs-Al$_x$Ga$_{1-x}$As[50], InAs-GaSb[50], HgTe-CdTe[51], and GaInAs-InP[52] with good success. Here we are interested in the intermixing effect in In$_{0.53}$Ga$_{0.47}$As/InP MQWs. Both Group III (Ga) and Group V (P) interdiffusion will be considered. Prior to the interdiffusion, the system is strain-free. After the interdiffusion, there is a weak strain distribution. Furthermore, with the interdiffusion, the system turns into a InGaAsP quaternary compound with compositional modulation. The strain distribution is related to the lattice mismatch by

$$\varepsilon_\parallel(z) = (a(z)-a_{InP})/a_{InP}$$

$$\varepsilon_{xx} = \varepsilon_{yy} = \varepsilon_\parallel \, , \, \varepsilon_{zz} = -(2C_{12}/C_{11}) \, \varepsilon_\parallel,$$

where $C_{12}$ and $C_{11}$ are the elastic constants which are position dependent. The effect of strain on the Hamiltonian will be modeled according to the Bir-Picus theory [53]. The strain Hamiltonian takes a diagonal form [in the EBOM basis labeled by

$(J,M)=(1/2,1/2),)(1/2,-1/2),(3/2,3/2),(3/2,1/2),(3/2,-1/2),(3/2,-3/2)]$ with the diagonal matrix elements given by

$$\Delta V_C, \Delta V_C, -\Delta V_H + D, -\Delta V_H - D, -\Delta V_H - D, \text{ and } -\Delta V_H + D,$$

where

$$\Delta V_C = 2c_1 \ (1-C_{12}/C_{11}) \ ) \ \varepsilon_{\parallel}$$

$$\Delta V_H = 2(a_1 + a_2) \ (1-C_{12}/C_{11}) \ ) \ \varepsilon_{\parallel}$$

and

$$D = b(2C_{12}/C_{11} + 1) \ \varepsilon_{\parallel}$$

The deformation potentials $(c_1 + a_1 + a_2)$ and b for InP, GaAs, and InAs can be found in Ref. [54]. For the alloys, we simply use the linear interpolation.

The input band parameters used in our modeling are listed in Table I. Here $E_v$ and $E_c$ are the zone-center energies for the valence band and conduction band, respectively. Note that we use the experimental bandgap of bulk $In_{0.53}Ga_{0.47}As$ as the input parameter rather than the linear interpolation of band gaps of InAs and GaAs, since the bandgap bowing effect is significant for InGaAs alloy.

The model system for the as-grown sample is a superlattice with each period consisting of 4 monolayers (11A) of $In_{0.53}Ga_{0.47}As$, one monolayer of $InAs_{0.5}P_{0.5}$ and 169 monolayers (497A) of InP. The presence of one monolayer of $InAs_{0.5}P_{0.5}$ is suggested by the DCXRD

analysis. Including this $InAs_{0.5}P_{0.5}$ monolayer at one interface between $In_{0.53}Ga_{0.47}As$ and InP in our model also makes the resulting energy gap (1.102eV) in better agreement with the PL measurement (1.082 eV). Without this $InAs_{0.5}P_{0.5}$ monolayer, the energy gap obtained in our model would have been 0.05eV higher. The difference of 20 meV between the theoretical band gap predicted here and the PL peak position can be attributed to the excitonic effect (which accounts for approximately 10 meV) and the effects due to difference in the realistic geometry and the ideal geometry used here. With intermixing, the system turns into a $In_{1-x}Ga_xAs_{1-y}P_y$ quaternary superlattice with both x and y being functions of z (the coordinate in growth direction). Since x is close to 0.47 in the well region and 0 in the barrier region, we obtain the EBOM parameters for $In_{1-x}Ga_xAs_{1-y}P_y$ by taking the linear interpolation between the corresponding EBOM parameters for $In_{0.53}Ga_{0.47}As_{1-y}P_y$ and $InAs_{1-y}P_y$ via the following relation

$$V(In_{1-x}Ga_xAs_{1-y}P_y) = (x/0.47)V(In_{0.53}Ga_{0.47}As_{1-y}P_y) + (1-x/0.47)V(InAs_{1-y}P_y),$$

where $V(In_{0.53}Ga_{0.47}As_{1-y}P_y) = (1-y)V(In_{0.53}Ga_{0.47}As) + yV(In_{0.53}Ga_{0.47}P)$

and $V(InAs_{1-y}P_y) = (1-y)V(InAs)+yV(InP).$

The composition (x or y) distribution is modeled by a simple diffusion theory [55]. For Group III (Ga) interdiffusion, we obtain

$$x = 0.47 \{erf[(L/2+z)/2\sqrt{D_1}t] + erf[(L/2-z)/2\sqrt{D_1}t]\}/2$$

and for Group V (P) interdiffusion, we have

$$y = 1- \{erf[(L/2+z)/2\sqrt{D_2}t] + erf[(L/2-z)/2\sqrt{D_2}t]\}/2$$

$$- 0.5 \{erf[(a_1/2+z_1)/2\sqrt{D_2}t] + erf[(a_1/2-z_1)/2\sqrt{D_2}t]\}/2,$$

where $D_1$ and $D_2$ are the diffusion constants for describing Ga and P interdiffusions, respectively and t is the annealing time. L is the width of the quantum well and z is distance measured from the center of the well. The second term in the expression for y(z) describes the interdiffusion due to the one monolayer $InAs_{0.5}P_{0.5}$ at the interface. In this term, $a_1$ denotes the thickness of the monolayer and $z_1$ is the distance measured from the center of the $InAs_{0.5}P_{0.5}$ monolayer. The diffusion constant is determined by fitting the calculated band gap energies to the experimental results. With $D_1 = 7.03 \times 10^{-17}$ cm$^2$/s and $D_2 = 3.92 \times 10^{-17}$ cm$^2$/s we obtain a very good fit to the PL data as shown in Fig. 17.
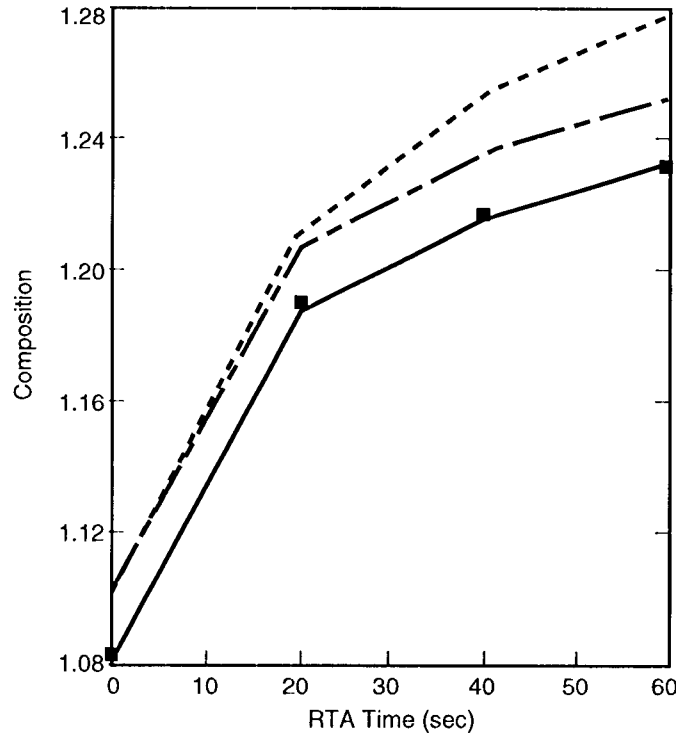


Figure 17. Calculated bandgap as a function of the annealing time at 800C. Dashed curve: with both P and Ga interdiffusion. Dotted curve: with P interdiffusion only. Filled squares: 6K photoluminescence data. The second solid line is just the first dashed curve down-shifted by 20 meV to match the experiment.

In Fig. 17, the dotted line shows the calculated band gap as a function of the annealing time with Group V (P) interdiffusion alone and the dashed line shows the results with both Group III and Group V interdiffusions. To compare with the PL data, we have rigidly shifted the calculated band gap by 20 meV downward so that the calculated results for as-grown sample agree with the PL data. We found that the Group III (Ga) interdiffusion has much smaller effect on the band gap shift compared with the Group V (P) interdiffusion. This also means that the diffusion constant for Group III interdiffusion obtained by fitting the PL data is subject to a much larger error. With the diffusion constants used, the resulting composition distributions for x(z) (solid curves) and y(z) (dashed curves) for different annealing times (t=20, 40, and 60 seconds) are shown in Fig. 18. Note that y(z) is not symmetric with respect to z because of the contribution from the monolayer $InAs_{0.5}P_{0.5}$ at the interface.
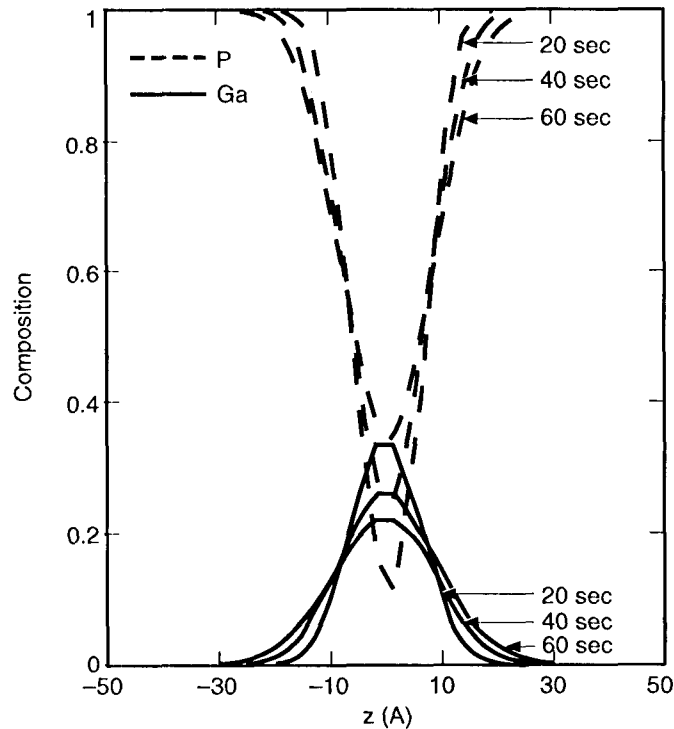
Figure 18. P (dashed line) and Ga (solid line) compositions versus z (the coordinate in growth direction).

## Conclusion

In conclusion, we have demonstrated that RTA can be employed to both shift the operating wavelength and to broaden the response of an ultra-thin p-type InGaAs/InP quantum well infrared photodetector following intermixing of the well and barrier layers during rapid thermal annealing. The use of RTA changes the well profile of a QWIP and peak wavelength, but the reduced responsivity indicates that this technique is limited for sensitive IR detectors. Recent advances in growth, complimented by innovative structures (random gratings and reflector layers) should offset any degradation in performance. This makes feasible integration of multiple-colored pixels.

## Acknowledgment

## References

1. L. Esaki and R. Tsu, IBM J. Res. Develop. 14, 61 (1970).

2. A.C. Gossard, P.M. Petroff, W. Wiegman, R. Dingle, and A. Savage, Appl. Phys. Lett. 29, 323 (1976)

3.  E.E. Mendez, L.L. Change, C.A. Chang, L.F. Alexander, and L. Esaki, Surf. Sci. 142, 215 (1984).

4.  Y.D. Galeuchel, P. Roentgen, and V. Graf, Appl. Phys. Lett. 53, 2638 (1988).

5.  K.Y. Cheng, A.Y. Cho, T.J. Drummond, and H. Morkoc, Appl. Phys. Lett. 40, 147 (1982).

6.  G.C. Osbourn, J. Appl. Phys. 53, 1586 (1982); G.C. Osbourn, R.M. Riefield, and P.L. Gourley, Appl. Phys. Lett. 41, 172 (1982).

7.  T.P. Pearsall, F.H. Pollak, and J.C. Bean, Bull. Am. Phys. Soc. 30, 266 (1985).

8.  A. Orchel, U. Cebulla, G.T. Pankle, H. Kroemer, S. Subbana, and G. Griffiths, Surf. Sci. 174, 143 (1986).

9.  G. Abstreiter, H. Brugger, T. Wolf, H. Jorke, and H.J. Herzog, Phys. Rev. Lett. 54, 2441 (1985).

10. J.N. Schulman and T.C. McGill, Appl. Phys. Lett. 34, 663 (1979).

11. J.P. Faurie, A. Millon, and J. Piaguet, Appl. Phys. Lett. 41, 713 (1982).

12. X.C. Zhang, S.K. Chang, A.V. Nurmikko, L.A. Kolodziejski, R.L. Gunshor, and S. Datta, Phys. Rev. 31, 4056 (1985).

13. L.A. Kolodziejski, R.L. Gunshor, T.C. Bonsett, R. Venkatasubramanian, S. Datta, R.B. Bylsma, W.M. Becker, and N. Otsuka, Appl. Phys. Lett. 47, 169 (1985).

14. G.H. Dohler, H. Kunzel, D. Oiego, K. Ploog, P. Ruden, H.J. Stolz, and G. Abstriter, Phys. Rev. Lett. 47, 864, (1981).

15. E. Caruthes and P.J. Lin-Chung, Phys. Rev. Lett. 39, 1543 (1977).

16. D. Ninno, K.B. Wong, M.A. Gell, and M. Jaros, Phys. Rev. B 32, 2700 (1985).

17. N.N. Schulman and T.C. McGill, Phys. Rev. Lett. 39, 1680 (1977).

18. J.N. Schulman and Y.C. Chang, Phys. Rev. B 24, 4445 (1981); Phys. Rev. B 27, 2346 (1983).

19. Y.T. Lu and L.J. Sham, Phys. Rev. B 40, 5567 (1989).

20. L.L. Chang and L. Esaki, Surf. Sci. 98, 70 (1980).

21. G. Bastard, Phys. Rev. 25, 7584 (1982).

22. G.D. Sanders and Y.C. Chang, Phys. Rev. B 31, 6892 (1985).

23. C. Mailhiot, D.L. Smith, and T.C. McGill, J. Vac. Sci. Technol. B2(3), 371 (1984).

24. D.Z.-Y. Ting and Y.C. Chang, Phys. Rev. B 36, 4357 (1987).

25. Y.C. Chang, Phys. Rev. B 37, 8215 (1988).

26. D. Ahn, S.L. Chuang and Y.C. Chang, J. Appl. Phys. 64, 4056 (1988).

27. D.A. B. Miller, D.S. Chemla, T.C. Damen, A.C. Gossard, W. Wiegmann, T.H. Wood, and C.A. Burrus, Appl. Phys. Lett. 45, 13 (1984).

28. D.S. Chemla and D.A.B. Miller, J. Opt. Soc. Am B2, 1155 (1985).

29. S. Schmitt-Rink and C. Ell, J. Lumimn. 30, 585 (1985).

30. B.F. Levine, G. Hasnain, C.G. Bethea, and N. Chand, Appl. Phys. Lett. 54, 27044 (1989).

31. B.F. Levine, J. Appl. Phys. 74, R1 (1993).

32. K.K. Choi, B.F. Levine, C.G. Betha, J. Walker, and R.J. Malik, Appl. Phys. Lett. 50, 1814 (1987).

33. T.H. Wood, R.W. Tkach, and A.R. Chraplyvy, Appl. Phys. Lett. 50, 798 (1987).

34. S. Weiner, D.A.B. Miller, and D.S. Chemla, Appl. Phys. Lett. 50, 842 (1987).

35. E. Efron, T.Y. Hsu, J.N. Schulman, W.Y. Wu, I. Rouse, I.J. D'Haenens, and Y.C. Chang, Proceedings of the SPIE Conference on Quantum Well and Superlattice Physics, Vol. 792, p. 197 (1987).

36. D.L. Smith, T.C. McGill, and J.N. Schulman, Appl. Phys. Lett. 43, 180 (1983).

37. G.D. Sanders and Y.C. Chang, Phys. Rev. B35, 1300 (1987).

38. S.D. Gunapala and S.V. Bandara, Physics of Thin Films, edited by M.H. Francombe, and J.L. Vossen, Vol. 21, pp. 113-237, Academic Press, N.Y., (1995).

39. B. Levine, J. Appl. Phys. 74, R1 (1993).

40. S.A. Lyon, Surf. Sci., Vol. 228, p. 508, (1990).

41.  S.D. Gunapala, J.S. Park, G. Sarusi, T.L. Lin, J.K. Liu, P.D. Maller, R.E. Muller, C.A. Shott, and T. Hoeltz, IEEE Trans on Electron Devices, Vol. 44, No. 1, Jan 1997.

42.  H.C. Liu, Optical Engineering 33 (J), 1961-1967 (1994).

43.  S.D. Gunapala, B.F. Levine, D. Ritter, R. Hamm and M.R. Danish, Appl. Phys. Lett. 58, 202-4 (1991).

44.  J.D. Ralston, M. Ramsteiner, B. Dischler, M. Maier, P. Koidl, and D.J. As, J. Appl. Phys. 70, 2195 (1991).

45.  D.G. Deppe and N. Holonyak, Jr., J. Appl. Phys. 64, R93 (1988).

46.  J. Beauvais, J.H. Marsh, A.H. Kean, A.C. Boyle, B. Garrett, and R.W. Celew, Electron Lett. 28, 1670 (1992).

47.  C.J. McLean, J.H. Marsh, R.M. DeLaRue, A.C. Boyle, B. Garrett, and R.W. Glen, Electron Lett. 28, 1117 (1992).

48.  S.L. Jackson, J.N. Ballargeon, A.P. Curtis, X. Liu, J.E. Burkes, J.I. Malin, K.C. Hseih, S.G. Bishop, K.Y. Cheng, and G.E. Stillman, J. Val. Sci. Technol. B11, 1045 (1993).

49.  W. Wu, S. Skala, J.R. Tucker, J.W. Lyding, A. Seabaugh, E.A. Beam III, and D. Joranovic, J. Vac. Sci. Technol. A13, b02 (1995).

50.  Y.C. Chang, Phys. Rev. B37, 8215 (1988).

51.  Y.C. Chang, J. Cheung, A. Chiou, and M. Khoshnerisan, J. Appl. Phys. 66, 829-834 (1989).

52.  M.P. Houng and Y.C. Chang, J. Appl. Phys. 65, 3092 (1989).

53.  G.L. Bir and G. E. Pikus, Symmetry and Static Induced Effects in Semiconductors (Halsted, United Kingdom, 1974).

54.  S. Adachi and C. Hamaguchi, Phys. Rev. B19, 938 (1979).

55.  Choy, J. Appl. Phys. 82, 3861 (1997).